JOURNAL OF PROPULSION AND POWER
Vol. 13, No. 4, July–August 1997

# Macroscopic Balance Model for Wave Rotors

Gerard E. Welch*
*NASA Lewis Research Center, Cleveland, Ohio 44135*

**A mathematical model for wave rotors is described. The wave processes that affect energy exchange within the rotor passages are modeled using one-dimensional gasdynamics. Macroscopic balances relate volume-averaged thermodynamic properties in the rotor passage control volume to the mass, momentum, and energy fluxes at the ports. Simple loss models are used to estimate entropy production in boundary layers and in separating flows caused by blade-blockage, incidence, and the gradual opening and closing of rotor passages. The mathematical model provides a basis for designing port and rotor geometry, and for predicting design-point wave rotor performance. Model predictions are evaluated through comparisons with computational fluid dynamics calculations and three-port wave rotor experimental data. A four-port wave rotor design example is provided to demonstrate model applicability. The modeling approach is amenable to wave rotor optimization studies and rapid assessment of the tradeoffs associated with integrating wave rotors into gas turbine engine systems.**

## Nomenclature

$A$ = area
$A_P$ = cross-sectional flow area at end of a rotor passage
$A_W$ = surface area (hub, tip, and shroud) of a rotor passage
$a$ = $[(\gamma - 1)h]^{1/2}$, local speed of sound
$a_{t,r}$ = $\{a^2 + [(\gamma - 1)/2]\boldsymbol{w}\cdot\boldsymbol{w}\}^{1/2} = [(\gamma - 1)h_{t,r}]^{1/2}$, local relative total speed of sound
$C_S$ = empirical constant (0.23), used in Eq. (18)
$\boldsymbol{e}_\theta$ = unit vector in tangential direction
$e$ = specific internal energy
$e_t$ = $e + \frac{1}{2}\boldsymbol{u}\cdot\boldsymbol{u}$, specific total internal energy
$e'_t$ = $e + \frac{1}{2}[\boldsymbol{w}\cdot\boldsymbol{w} - (r\Omega)^2]$, specific relative total energy
$f_b$ = $(\dot{m}_{\text{in}} - \dot{m}_{\text{ex}})/\dot{m}_{\text{in}}$, coolant bleed fraction
$f(\zeta)$ = momentum function, Eq. (12)
$g(\zeta)$ = energy function, Eq. (13)
$HR$ = ratio of outlet to inlet port absolute total enthalpies
$HR'$ = ratio of outlet to inlet port relative total enthalpies
$h$ = $e + p/\rho$, specific enthalpy
$h_t$ = $h + \frac{1}{2}\boldsymbol{u}\cdot\boldsymbol{u}$, specific total enthalpy
$h'_t$ = $h_t - u_\theta r\Omega$, specific rothalpy
$h_{t,r}$ = $h_t - \frac{1}{2}(\boldsymbol{u}\cdot\boldsymbol{u} - \boldsymbol{w}\cdot\boldsymbol{w})$, specific relative total enthalpy
$L_T$ = rotor chord length
$M_S$ = relative shock Mach number, Eq. (20)
$M_x$ = relative Mach number of incoming flow relative to shock wave
$M_{\Omega,\text{in}}$ = $[\langle r\Omega\rangle^2/(\gamma - 1)(h_t)_{\text{in}}]^{1/2}$, rotor Mach number
$m$ = mass
$\dot{m}$ = mass flow rate time-averaged over one wave cycle
$\boldsymbol{n}$ = local unit normal of control volume surface
$n$ = number of wave cycles experienced by a passage in one rotor revolution, i.e., number of duct sets
$p$ = static pressure
$p_t$ = total pressure
$p_{t,r}$ = relative total pressure
$\boldsymbol{q}$ = heat flux vector
$q'''$ = volumetric heat generation rate
$R_H$ = rotor hub radius
$R_T$ = rotor tip radius
$\boldsymbol{r}$ = $(r, \theta, x)$, position vector
$T_t$ = absolute total temperature
$t$ = time
$t_i$ = $i$th wave time, Fig. 3
$t_V$ = $L_T/[(\gamma - 1)(h_{t,r})_V]^{1/2}$, reference time
$\boldsymbol{u}$ = $(u_r, u_\theta, u_x)$, local fluid velocity
$\boldsymbol{u}_s$ = local velocity of control volume surface
$V$ = volume
$V_P$ = volume of a rotor passage
$w$ = $|\boldsymbol{w}|$, fluid speed in rotor frame of reference
$\boldsymbol{w}$ = $\boldsymbol{u} - r\Omega\boldsymbol{e}_\theta = (w_r, w_\theta, w_x)$, local relative fluid velocity
$\alpha_e$ = $(mh_{t,r})_{\text{out}}/(mh_{t,r})_V$, energy discharge fraction, Eq. (11)
$\alpha_m$ = $m_{\text{out}}/m_V$, mass discharge fraction, Eq. (9)
$\alpha_p$ = momentum integral, Eq. (10)
$\alpha_w$ = momentum integral, Eq. (10)
$\beta$ = $\dot{m}_{\text{hi}}/\dot{m}_{\text{in}}$, divider cycle mass flow rate fraction
$\beta_f$ = $\tan^{-1}(\langle w_\theta\rangle/\langle w_x\rangle)$, local relative flow angle
$\beta^*$ = local blade angle defined positive from rotor axis in direction of rotation
$\gamma$ = ratio of specific heats
$\Delta s/R$ = normalized entropy production
$\varepsilon$ = $p_e/p_V$, principal expansion fan pressure ratio
$\zeta$ = $t_b/t_a$
$\eta_{\text{out}}$ = $\ell n[(\alpha_e/\alpha_m)^{\gamma/(\gamma-1)}]/\ell n[(p_{t,r})_{\text{out}}/p_V]$, low-pressure exhaust port discharge process polytropic efficiency
$\rho$ = fluid mass density
$\tau_{\text{cycle}}$ = $(2\pi)/(n\Omega)$, wave rotor cycle time
$\psi$ = $\langle w_x\rangle/\langle r\Omega\rangle$, local flow coefficient
$\Omega$ = shaft angular speed

*Subscripts*
bl = entropy production in boundary layers
$C$ = fresh air portion of state $Q$
cs = entropy production in coalescing shock wave
$D$ = undischarged gas portion of state $Q$
$e$ = uniform velocity region of low-pressure exhaust port, corresponding to times $t_a \le t \le t_b$
hi = divider cycle high-pressure exhaust port
in = wave rotor inlet port, divider cycle medium pressure port or four-port cycle low-pressure inlet port
lo = divider cycle low-pressure exhaust port
out = wave rotor outlet port
$Q$ = state of gas in rotor passage following the low-pressure port region of wave cycle

Presented as Paper 96-0243 at the AIAA 34th Aerospace Sciences Meeting, Reno, NV, Jan. 15–19, 1996; received April 5, 1996; revision received March 7, 1997; accepted for publication March 28, 1997. This paper is declared a work of the U.S. Government and is not subject to copyright protection in the United States.

*Aerospace Engineer, Vehicle Technology Center, U.S. Army Research Laboratory, 21000 Brookpark Road, M/S 77-6. Member AIAA.

$S$ = entropy production in shock wave
$V$ = reference conditions, i.e., the conditions in the rotor passage just prior to low-pressure exhaust port

*Special Symbols*
$*$ = nondimensional value
$-$ = volume-averaged quantity
$\langle\,\rangle$ = mass-averaged quantity

## Introduction

THE wave rotor is a rotating machine that uses gasdynamic waves to exchange energy between gas streams of differing energy density. As shown in Fig. 1, a shrouded rotor is surrounded by a stationary casing. The casing end walls are penetrated by inlet and outlet ports that carry the gas to and from the rotor passages. At any time, sectors of the rotor flow annuli are exposed to the ported flows while the remaining sectors face the casing end walls. The gasdynamic waves that affect the energy exchange are initiated as the rotor passages open and close to the ported flows in a timed sequence, dictated by the azimuthal location and extent of the ports and the rotor speed. At an inlet port, low-pressure gas in the rotor passage is exposed to the high-pressure port flow; a compression wave (which eventually steepens into a shock wave), compresses the passage gas and, thus, allows the incoming gas to enter the rotor. At an exhaust port, high-pressure passage gas is suddenly exposed to the low-pressure exhaust port flow; an expansion wave propagates into the rotor passage, reduces the passage pressure, and discharges the passage gas into the exhaust port. Various gas cycles are affected by sequential charge and discharge processes established by the port timing; these include three-port divider cycles[1,2] and multiport cycles for gas turbine engine topping applications.[3–6] The interesting history of wave rotor and its applications is documented in Refs. 7–12.

A current effort is aimed at applying wave rotor technology to increase the performance of gas turbine engines.[13] Much of this effort is devoted to computational fluid dynamics (CFD) tool development[14–16] to simulate accurately wave rotor flow dynamics. The purpose of this paper is to describe a mathematical model that provides accurate design-point wave rotor performance while using significantly less computational investment than nominally required by CFD tools. The model is suitable for preliminary port timing, duct angle estimates, and rotor geometry optimization. The modeling approach provides a tool for rapid assessment of the tradeoffs associated with integrating wave rotors into gas turbine engines.

The paper is arranged as follows: The mathematical model is first described. Model predictions are then compared with CFD results and three-port experimental data. Finally, the model is used to design a four-port wave rotor for a small turboshaft engine topping cycle as a demonstration of model applicability.

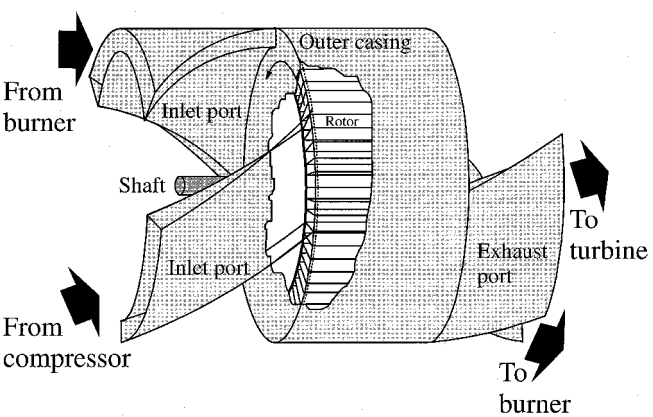


**Fig. 1 Four-port wave rotor schematic diagram.**

## Mathematical Model

### Overview

The wave rotor model has three principal elements: 1) macroscopic balances that enforce global mass and energy conservation in a wave rotor passage as it rotates between strategically defined end-states within a prescribed wave cycle; 2) one-dimensional gasdynamic wave calculations that establish the port timing and the mass, momentum, and energy fluxes at the passage ends; and 3) entropy production models for principal wave rotor loss mechanisms. The gas is assumed to be at rest in the rotor frame of reference at the defined end-states; the gas in these states can be nonuniform and discontinuous. Gas particles within the rotor are assumed to travel at a constant radius and the cross-sectional flow area of the passages is assumed constant. The working fluid is treated as a perfect gas with a constant ratio of specific heats $\gamma$.

The macroscopic balances are developed in the next section. The gasdynamic wave processes and timing, and the entropy production mechanisms inherent to the wave cycle are then described. Finally, other important wave rotor entropy production mechanisms are discussed.

### Macroscopic Balances

The conservation of mass for a generalized control volume $V$ requires that

$$\frac{\mathrm{d}}{\mathrm{d}t}\int_{V(t)} \rho\,\mathrm{d}V = -\int_{A(t)} \rho(\boldsymbol{u}-\boldsymbol{u}_s)\cdot n\,\mathrm{d}A \tag{1}$$

The conservation of energy (neglecting work rates resulting from body and shear forces) requires that

$$\frac{\mathrm{d}}{\mathrm{d}t}\int_{V(t)} \rho e_t\,\mathrm{d}V = -\int_{A(t)} \rho h_t(\boldsymbol{u}-\boldsymbol{u}_s)\cdot\boldsymbol{n}\,\mathrm{d}A - \int_{A(t)} p\boldsymbol{u}_s\cdot\boldsymbol{n}\,\mathrm{d}A - \int_{A(t)} \boldsymbol{q}\cdot\boldsymbol{n}\,\mathrm{d}A + \int_{V(t)} q'''\,\mathrm{d}V \tag{2}$$

where $e_t \equiv e + \frac{1}{2}\boldsymbol{u}\cdot\boldsymbol{u}$ is the specific total energy, $h_t \equiv e_t + p/\rho$ is the specific total enthalpy, and $\int p u_s\cdot\boldsymbol{n}\,\mathrm{d}A$ is the boundary work rate. By using the conservation of angular momentum

$$\frac{\mathrm{d}}{\mathrm{d}t}\int_{V(t)} \rho u_\theta r\Omega\,\mathrm{d}V = -\int_{A(t)} \rho\boldsymbol{u}_\theta r\Omega(\boldsymbol{u}-\boldsymbol{u}_s)\cdot n\,\mathrm{d}A - \int_{A(t)} pr\Omega\boldsymbol{e}_\theta\cdot\boldsymbol{n}\,\mathrm{d}A \tag{3}$$

where $r$ is radius, and $u_\theta$ is the local tangential velocity component. Equation (2) is rewritten as

$$\frac{\mathrm{d}}{\mathrm{d}t}\int_{V(t)} \rho e_t'\,\mathrm{d}V = -\int_{A(t)} \rho h_t'(\boldsymbol{u}-\boldsymbol{u}_s)\cdot\boldsymbol{n}\,\mathrm{d}A - \int_{A(t)} p(\boldsymbol{u}_s - r\Omega\boldsymbol{e}_\theta)\cdot\boldsymbol{n}\,\mathrm{d}A - \int_{A(t)} \boldsymbol{q}\cdot\boldsymbol{n}\,\mathrm{d}A + \int_{V(t)} q'''\,\mathrm{d}V \tag{4}$$

where $e_t' \equiv e + \frac{1}{2}[\boldsymbol{w}\cdot\boldsymbol{w} - (r\Omega)^2]$, $h_t' \equiv e_t' + p/\rho$, and $\boldsymbol{w} \equiv \boldsymbol{u} - r\Omega\boldsymbol{e}_\theta$. The energy $e_t'$ is by definition uninfluenced by shaft work rate [in Eq. (3)].

Equation (4) elicits an interesting description of the wave rotor energy exchange process. Consider two adjacent control volumes within a rotor passage that share a boundary that moves with some relative velocity component $w$, normal to the passage cross-sectional area $A$, across which pressure $p$ is continuous (e.g., a contact discontinuity or particle path). The rate

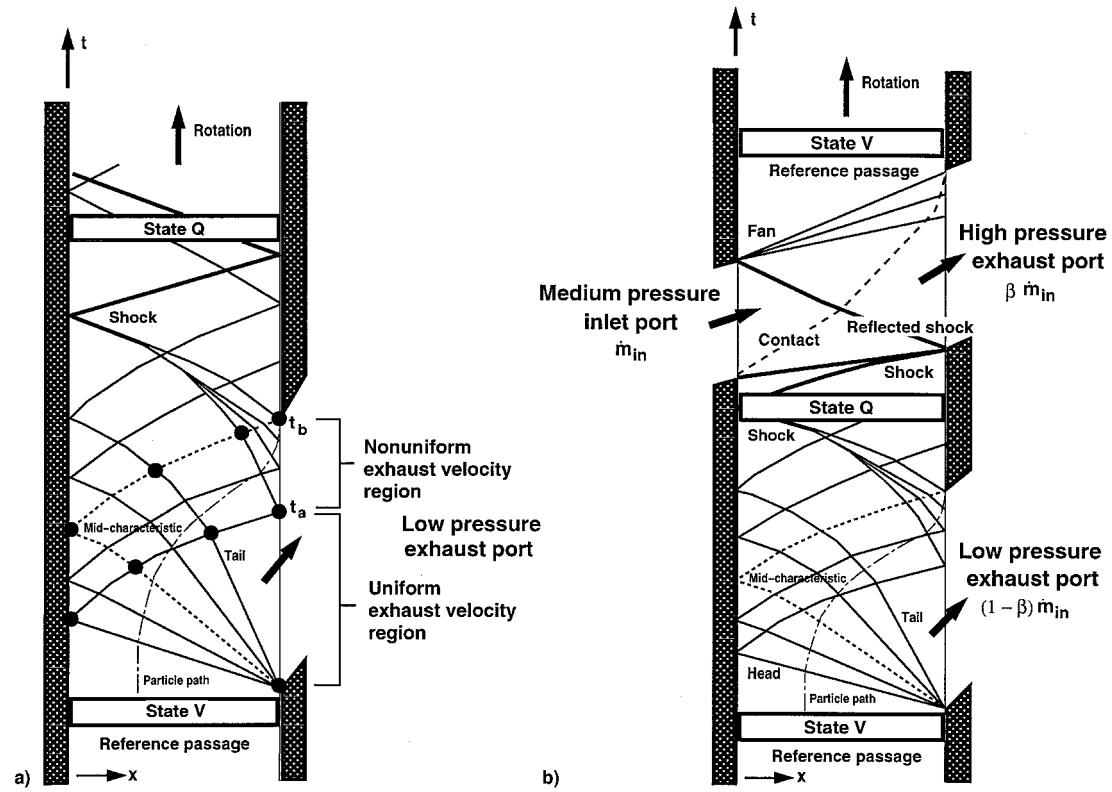


**Fig. 2 Position-time diagrams for a) wave rotor passage exhaust process and b) three-port divider cycle.**

at which relative total energy is added to one of the control volumes by the boundary work rate ($\int pw\ \mathrm{d}A$) is by definition equal to the rate at which energy is extracted from the adjacent control volume by boundary work ($-\int pw\ \mathrm{d}A$); i.e., the energy exchange between the two control volumes is manifested through the boundary work rate term in the macroscopic balance description and does not explicitly depend on the gasdynamic waves instantaneously captured within either of the control volumes. If now the control volume is defined to encompass the full rotor passage, the boundary work rate term of Eq. (4) is zero (because $\boldsymbol{u}_S = r\Omega\hat{\boldsymbol{e}}_\theta$), and the rate of change of the relative total energy within the rotor passage depends only on the net flux of rothalpy ($h_t'$) through the passage ends, heat transfer, and the volumetric heat generation rate.

Equations (1) and (4) can be integrated between two times $t_1$ and $t_2$ (or azimuthal position given that $\mathrm{d}\theta = \Omega\ \mathrm{d}t$), to give

$$m_2 = m_1 + \left(\int_{A_P}\int_{t_1}^{t_2} \rho u_x\ \mathrm{d}t\ \mathrm{d}A\right)_{\text{in}} - \left(\int_{A_P}\int_{t_1}^{t_2} \rho u_x\ \mathrm{d}t\ \mathrm{d}A\right)_{\text{out}} \tag{5}$$

where $m = \bar{\rho}V_P$ is the mass of the gas contained in the passage control volume $V_P$. By integrating Eq. (4) between the same times, the conservation of relative total energy yields

$$\bar{p}_2 = \bar{p}_1 + \frac{\gamma - 1}{V_P}\left[\left(\int_{A_P}\int_{t_1}^{t_2} \rho u_x h_{t,r}\ \mathrm{d}t\ \mathrm{d}A\right)_{\text{in}} - \left(\int_{A_P}\int_{t_1}^{t_2} \rho u_x h_{t,r}\ \mathrm{d}t\ \mathrm{d}A\right)_{\text{out}} - \int_{A_W}\int_{t_1}^{t_2} \boldsymbol{q}\cdot\boldsymbol{n}\ \mathrm{d}t\ \mathrm{d}A + \int_{V_P}\int_{t_1}^{t_2} q'''\ \mathrm{d}t\ \mathrm{d}V\right] \tag{6}$$

provided that the gas at states 1 and 2 is at rest ($\boldsymbol{w}\cdot\boldsymbol{w} = 0$) relative to the rotor. The relative total enthalpy is given by $h_{t,r} = h_t' + \frac{1}{2}(r\Omega)^2$, $\bar{p}$ is volume-averaged static pressure, and $u_x(=w_x)$ is the through-flow component of velocity. The wave rotor is time-periodic; hence, if $t_2$ is chosen as $t_2 = t_1 + n\tau_{\text{cycle}}$, then Eqs. (5) and (6) express mass and relative energy conservation for the machine. An analogous application of Eq. (3) provides an expression for wave rotor shaft power.

It is convenient to nondimensionalize by the reference state properties $\rho_V = m_V/V_P$ and $a_V \equiv [(\gamma - 1)h_V]^{1/2}$. The nondimensional density $\rho_V^*$ and speed of sound $a_V^*$ in the reference state are both defined as unity, and, by the equation-of-state ($\gamma p = \rho a^2$), the nondimensional static (and relative stagnation) pressure $p_V^*$ is therefore $1/\gamma$. Lengths are normalized by $L_T$, and thus, time is conveniently normalized by the time for a sound wave to traverse the rotor in the reference state, $t_V = L_T/a_V$.

### Wave Processes and Timing

The port timing, i.e., the leading and trailing azimuthal positions of the ports, is set by the specified wave position-time ($x$–$t$) diagram and the speed of the gasdynamic waves that affect the energy transfer in the wave rotor passages. Isentropic compression and expansion waves are treated by using the invariance of Riemann variables along their characteristics and across waves of the opposite gender (cf., Ref. 17). The Rankine–Hugoniot relations are used to calculate shock speeds, compression ratios, and inherent entropy production. All wave speeds are calculated with one-dimensional gasdynamics in which pitchwise and spanwise flowfield variations are neglected; further, the predicted wave speeds are not influenced by local flow losses (e.g., boundary-layer attenuation of shock speed) or multidimensional effects (e.g., the gradual, rather than instantaneous, opening and closing of passages). Global loss mechanisms do, however, influence timing through their influence on the mass-averaged entropy of the control volume. The modeling presented in this section includes entropy production inherent in shock waves and that introduced in mixing nonuniform exhaust port flowfields. Other wave rotor loss mechanisms are discussed later.

#### *Low-Pressure Exhaust Port*

The gas in the (reference) passage about to open to the low-pressure exhaust port (Fig. 2a) is uniform and at rest in the

**Table 1 Comparison of calculated exhaust-port nondimensional values for an instantaneously opened rotor passage at $g = 1.4$ and $\varepsilon = 0.353$ (Ref. 17)**

| | $t_a/t_V$ | $t_b/t_V$ | $m_{\text{out}}/m_V$ | $(mh_{t,r})_{\text{out}}/(mh_{t,r})_V$ | $(p_{t,r})_{\text{out}}/p_V$ | $\eta_{\text{out}}$ |
|---|---|---|---|---|---|---|
| Present model | 1.737[a] | 2.588 | 0.692[b] | 0.574[c] | 0.506[d] | 0.965[e] |
| MOC [17] | ≃1.77 | ≃2.66 | ≃0.72 | —— | —— | —— |
| One-dimensional CFD [14] | 1.724 | 2.600 | 0.692 | 0.574 | 0.505 | 0.961 |
| Analytical | 1.7342 | —— | —— | —— | —— | —— |

[a]$t_a/t_V$ and $t_b/t_V$ are from three-wave MOC calculation. [b]From Eq. (9). [c]From Eq. (11). [d]Mixed-out total pressure using Eqs. (7–14). [e]Polytropic efficiency, $\eta_{\text{out}} \equiv [\gamma/(\gamma-1)]\ell n(\alpha_e/\alpha_m)/\ell n[(p_{t,r})_{\text{out}}/p_V]$.

rotor frame of reference ($\boldsymbol{w} = 0$). The exhaust process is characterized by $\varepsilon$, or the ratio of the uniform static pressure $p_e$, at the interface between the rotor and the low-pressure port to the initial passage pressure $p_V$. The principal expansion fan initiated at $t = 0$ reflects off the wall ($x = 0$), and the head (leading characteristic) of the reflected fan arrives back at the exhaust port at $t = t_a$. In the uniform region $0 \le t \le t_a$, the passage gas is discharged with uniform axial velocity (here assuming inviscid flow) given by

$$\frac{w(0 \le t \le t_a)}{a_V} = \frac{w_e}{a_V} = \frac{2}{\gamma - 1}\left[1 - \varepsilon^{(\gamma-1)/2\gamma}\right] \tag{7}$$

where $w = |\boldsymbol{w}|$. The reflected fan reduces the exhaust port discharge velocity and establishes the nonuniform velocity region ($t_a \le t \le t_b$) noted in Fig. 2a. The exhaust port is closed (at time $t_b$), when the velocity in the exhaust port reaches zero, which corresponds to the time when the midcharacteristic of the principal expansion fan (shown in Fig. 2a) arrives back at the exhaust port. Although the time at which the head of the expansion fan reaches the exhaust port $t_a$ can be attained analytically, recourse to the method-of-characteristics[17] provides the port closing time $t_b$. The coarse method-of-characteristics (MOC) calculation involves the head, tail, and midcharacteristic of the expansion fan. The characteristics are treated as straight lines connecting the nine nodes identified in Fig. 2a. The slope (propagation velocity) of each line is based on the average of the wave speeds at the two connected nodes. The discharge velocity in the nonuniform region between the reflected head and midcharacteristic of the fan ($t_a \le t \le t_b$) is well approximated by

$$\frac{w(t_a \le t \le t_b)}{a_V} = \frac{w_e}{a_V}\frac{t_a}{(t_b - t_a)}\left(\frac{t_b}{t} - 1\right) \tag{8}$$

which was derived by assuming that the reflected fan in this region can be represented by a centered fan that reduces the discharge velocity from $w_e$ at $t_a$ to zero at $t_b$. By knowing the times $t_a$ and $t_b$, and by assuming isentropic expansion (i.e., neglecting entropy production internal to the passages for the moment), the following mass, momentum, and relative total energy integrals can be obtained:

$$\alpha_m \equiv \frac{m_{\text{out}}}{m_V} = \int_0^{t_b^*} \rho^* w^*\, dt^* = \frac{\rho_e}{\rho_V}\frac{w_e}{a_V}\frac{t_a}{t_V}\frac{\zeta\, \ell n\, \zeta}{(\zeta - 1)} \tag{9}$$

$$(\alpha_w, \alpha_p) = \int_0^{t_b^*} (\rho^* w^* w^*, p^*)\, dt^* = \left[\frac{\rho_e}{\rho_V}\frac{w_e^2}{a_V^2}\frac{t_a}{t_V} f(\zeta),\ \zeta\frac{p_e}{\gamma p_V}\frac{t_a}{t_V}\right] \tag{10}$$

$$\alpha_e = \frac{(mh_{t,r})_{\text{out}}}{(mh_{t,r})_V} = \int_0^{t_b^*} \rho^* w^* (a_{t,r}^*)^2\, dt^* = \alpha_m\left[\frac{a_e^2}{a_V^2} + \frac{\gamma - 1}{2}\frac{w_e^2}{a_V^2} g(\zeta)\right] \tag{11}$$

where $\zeta \equiv t_b/t_a$, $\rho_e/\rho_V = \varepsilon^{1/\gamma}$, $a_e^2/a_V^2 = \varepsilon^{(\gamma-1)/\gamma}$, given that $p_e/p_V = \varepsilon$. $\alpha_m \equiv m_{\text{out}}/m_V$ and $\alpha_e \equiv (mh_{t,r})_{\text{out}}/(mh_{t,r})_V$ are mass and energy discharge fractions, respectively, and

$$f(\zeta) \equiv 1 + \frac{\zeta}{(\zeta - 1)^2}(\zeta - \zeta^{-1} - 2\, \ell n\, \zeta) \tag{12}$$

$$g(\zeta) \equiv \frac{1 - \zeta^{-1} + (\zeta - 1)^{-2}[\frac{3}{2} + \frac{1}{2}\zeta^2 - 3\zeta + \zeta^{-1} + 3\, \ell n\, \zeta]}{\ell n\, \zeta} \tag{13}$$

Mixed-out exhaust port properties are calculated by solving for the uniform flowfield, that in time $t_b$ discharges the mass ($\cos\beta_{\text{out}}^*\alpha_m$), axial momentum [$(\cos\beta_{\text{out}}^*)^2\alpha_w + \alpha_p$], tangential momentum ($\cos\beta_{\text{out}}^* \sin\beta_{\text{out}}^*\alpha_w$), and energy [$\cos\beta_{\text{out}}^*\alpha_e/(\gamma - 1)$] calculated by using Eqs. (7–13), where $\beta_{\text{out}}^*$ is the blade angle on the low-pressure exhaust port end of the rotor. This analytical procedure[18] for constant area mixing provides explicit expressions for the mixed-out flow variables, including the mixed-out relative total pressure [$(p_{t,r})_{\text{out}}$]. Table 1 compares results of the present work with an MOC calculation,[17] a one-dimensional CFD calculation,[14] and analytical values for an example pressure ratio of $\varepsilon = 0.353$ (chosen in Ref. 17). Note that although the expansion fan process is assumed to be isentropic, the entropy production implied in the mixing to a uniform exhaust port flow (see more detailed discussion of mixing loss and its influence on the selection of design-point $\varepsilon$ in Ref. 19) is evidenced by the 96.5% polytropic efficiency $\eta_{\text{out}} \equiv [\gamma/(\gamma - 1)]\ell n(\alpha_e/\alpha_m)/\ell n[(p_{t,r})_{\text{out}}/p_V]$.

*Low-Pressure Inlet Port*

A pressure-exchanger is a wave rotor with axially aligned, uncambered blades in which design-point shaft power is (ideally) zero. Two-port pressure-exchangers with combustion internal to the passages[3] and four-port pressure-exchangers[20,21] proposed for topping gas turbine engines use the low-pressure inlet and outlet port arrangement shown in Fig. 3 to provide pressure gain: The mixed-out total pressure of the low-pressure exhaust port [$(p_t)_{\text{out}}$] is higher than the inlet port total pressure [$(p_t)_{\text{in}}$]. The ratio of the outlet and inlet port absolute total pressures is a function of the ratio of the absolute total enthalpies [$HR \equiv (h_t)_{\text{out}}/(h_t)_{\text{in}}$] in these ports, the mass ($\alpha_m$) and energy ($\alpha_e$) discharge fractions (both of which are functions of $\varepsilon$), $M_{\Omega,\text{in}}$, the coolant bleed fraction ($f_b \equiv (\dot{m}_{\text{in}} - \dot{m}_{\text{out}})/\dot{m}_{\text{in}}$), $\gamma$, and the machine loss levels.

As shown in Fig. 3a, the principal expansion fan reduces the passage pressure at the inlet port ($x = 0$) end of the machine. The passage opens to the inlet port soon after the passage pressure at the inlet end of the rotor is lower than the inlet port relative total pressure $(p_{t,r})_{\text{in}}$. The inflow gas is subsequently compressed by the shock formed by the coalescing compression waves produced as the principal expansion wave reflects off the nonuniform portion of the low-pressure exhaust port. State $Q$, which in Figs. 2a and 2b contains only the fraction of state $V$ gas that is not discharged from the exhaust port, has two constituents (as shown in Fig. 3): State $C$ contains the compressed fresh air from the inlet port, and state $D$ contains the undischarged state $V$ gas.

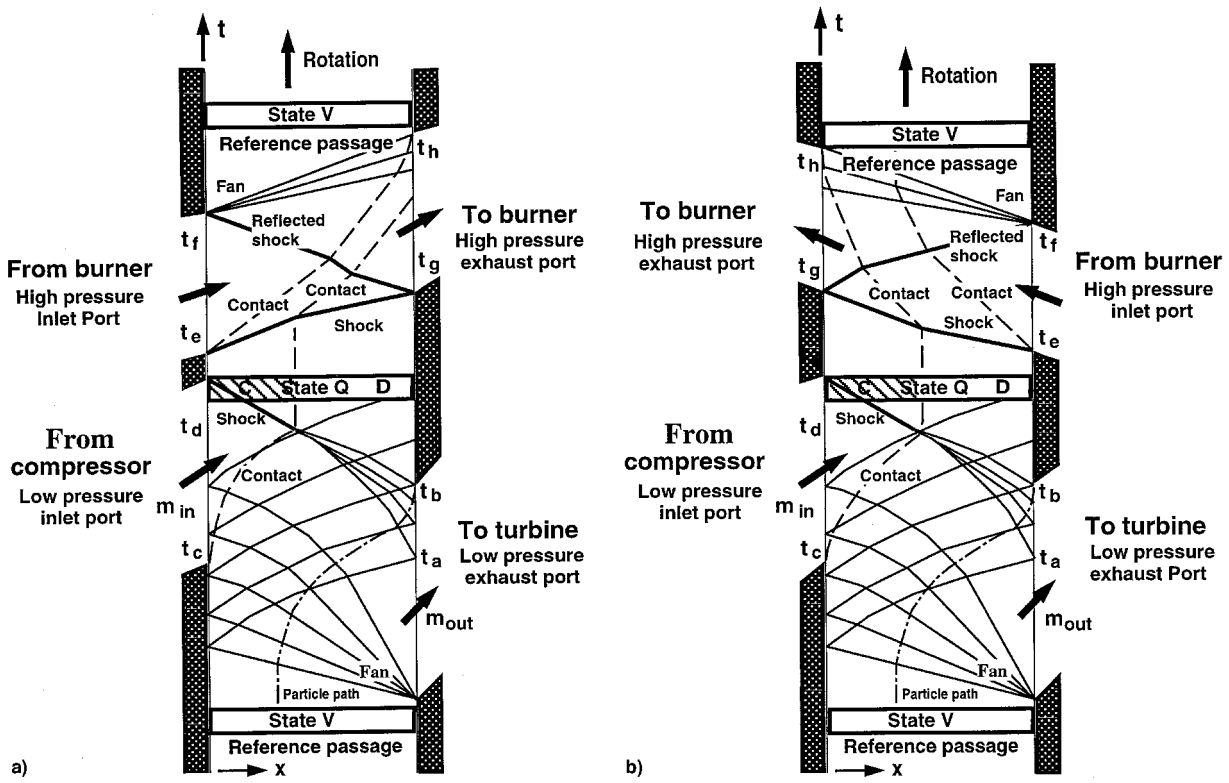


**Fig. 3 Position-time diagrams for a) through-flow four-port wave cycle and b) reverse-flow four-port wave cycle.**

By imposing the macroscopic balances [Eqs. (5) and (6)] on a passage moving from state $V$ to state $Q$ (which contains states $C$ and $D$), the volume-averaged density $\bar{\rho}_Q$ and the volume-averaged relative total (or static) pressure $\bar{p}_Q$ are obtained as

$$\frac{\bar{\rho}_Q}{\rho_V} = \frac{m_Q}{m_V} = 1 + \alpha_m \left( \frac{f_b}{1 - f_b} \right) \tag{14}$$

$$\frac{\bar{p}_Q}{p_V} = 1 - \gamma \alpha_e \left( 1 - \frac{1}{(1 - f_b) HR'} \right) \tag{15}$$

where $HR'$ is given by

$$HR' = \frac{HR - [(\gamma - 1)/2] M^2_{\Omega,\text{in}} [2\psi \tan \beta_f + 1]_{\text{out}}}{1 - [(\gamma - 1)/2] M^2_{\Omega,\text{in}} [2\psi \tan \beta_f + 1]_{\text{in}}} \tag{16}$$

where $\psi \equiv \langle w_x \rangle / \langle r\Omega \rangle$ is the local flow coefficient. The port angles are ideally set so that at the design point $\tan \beta_f \equiv \langle w_\theta \rangle / \langle w_x \rangle = \tan \beta^*$, where $\beta^*$ is the local blade angle (zero for a pressure-exchanger and, in general, nonzero for a wave engine[12,22]); $\langle w_x \rangle$, $\langle w_\theta \rangle$, and $\langle r\Omega \rangle$ are the mass-averaged axial velocity, relative tangential velocity, and rotor speed, respectively. The mass-averaged internal energy in state $D$ is related to that in state $V$ by the model expansion process

$$\frac{a^2_D}{a^2_V} = \left( \frac{\bar{p}_Q}{p_V} \right)^{(\gamma - 1)/\gamma} e^{\Delta s_{\text{bl}}/R} e^{\Delta s_{\text{cs}}/R} \tag{17}$$

$\Delta s_{\text{bl}}/R$ is the mass-averaged entropy production in boundary layers during the exhaust port discharge process (see Ref. 19 for a detailed discussion), and $\Delta s_{\text{cs}}/R$ is the entropy produced as the undischarged fraction of state $V$ gas is compressed by the coalesced waves reflected from the nonuniform region of the exhaust port. This is estimated by using

$$\Delta s_{\text{cs}}/R = C_s \Delta s_S [(a_{\text{out}}/a_{\text{in}})^2 M^2_{x,\text{in}}]/R \tag{18}$$

where $\Delta s_S(M^2_x)/R$ is the entropy production in a shock with a relative inflow Mach number $M_x$, $a_{\text{in}}$ and $a_{\text{out}}$ are the (mixed-out) speeds of sound in the inlet and outlet ports, respectively, $M_{x,\text{in}}$ is the Mach number of the inlet port flow relative to both the rotor and the reflected shock wave region $C$ air, and $C_S$ is an empirical constant (0.23) set by comparisons with one-dimensional CFD results (Fig. 4). By knowing the internal energy in state $D$, and by using the volume-averaged static pressure of state $Q$ calculated earlier, the density of the fluid in state $D$ can be calculated. By recognizing that the mass of fluid in state $D$ is the mass of the undischarged fraction of state $V$ gas, the (average) position of the contact separating states $C$ and $D$ can be calculated. The volume-averaged density in state $C$ can be calculated by knowing the position of the interface between states $C$ and $D$ and by knowing that the mass in state $C$ equals $m_{\text{in}}$. The internal energy in state $C$ can then be calculated by using the equation-of-state, given that the volume-averaged density in state $C$ and the volume-averaged pressure $\bar{p}_Q$ are known. The relative total enthalpy $(h^*_{t,r})_{\text{in}}$ in the rotor inlet port is known in terms of the relative total enthalpy ratio $[HR'$ of Eq. (16)] and the outflow relative total enthalpy $(h^*_{t,r})_{\text{out}} = \alpha_e/\alpha_m$; the ratio of the relative total enthalpies across the coalesced shock can thus be calculated using the shock relations

$$\frac{(h_{t,r})_C}{(h_{t,r})_{\text{in}}} = \frac{1 + [(\gamma - 1)/2](M^2_{x,\text{in}} - M^2_S)}{1 + [(\gamma - 1)/2](M_{x,\text{in}} + M_S)^2} \tag{19}$$

$$M^2_S = \frac{2}{\gamma - 1} \left\{ 1 + \frac{\gamma - 1}{2} M^2_{x,\text{in}} - \left[ 1 + \frac{2\gamma}{\gamma + 1} (M^2_{x,\text{in}} - 1) \right] \left[ 1 - \frac{2}{\gamma + 1} (1 - 1/M^2_{x,\text{in}}) \right] \right\}$$

where $M_S$ is negative (for the port orientation shown in Fig. 3). The properties in state $C$ were calculated earlier; by now having obtained $M_{x,\text{in}}$, the static and total properties and the

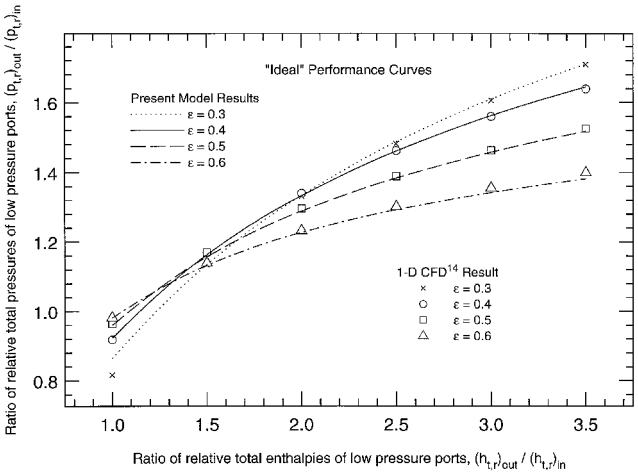


**Fig. 4 Comparison of the ratio of low-pressure exhaust port to low-pressure inlet port relative total pressures $(p_{t,r})_{out}/(p_{t,r})_{in}$ as a function of the ratio of the relative total enthalpies $(h_{t,r})_{out}/(h_{t,r})_{in}$ in the same ports, and $\varepsilon$, computed by using the present model and the one-dimensional CFD code of Ref. 14.**

average through-flow velocity in the inlet port can be calculated. The mass entering the inlet port is related to the mass discharged to the exhaust port by the specified coolant bleed fraction $f_b$; therefore, the total time that the inlet port is open $t_{in}$ can be calculated. The inlet port is closed when the coalesced shock reaches the inlet side of the rotor $x = 0$. This time $t_d$ is that for a sound wave to traverse state $D$, plus the time for the coalesced shock wave to traverse state $C$, plus the time that the exhaust port is open $t_b$; the inlet port, therefore, opens (at $t_c$) a time $t_{in}$ earlier than the closing time $t_d$.

Predictions of the ratio of the outlet and inlet port relative total pressures as a function of the outlet and inlet port relative total enthalpies, and the principal expansion fan pressure ratio ($\varepsilon \equiv p_e/p_V$) from the present model and from the one-dimensional CFD code of Ref. 14 are compared in Fig. 4. Only shock and nonuniform port flow mixing losses are accounted for in these ideal inviscid calculations, in which all other wave rotor loss mechanisms are neglected; the loss models of the CFD code are similarly disabled. The excellent agreement shown in Fig. 4 builds confidence in the present model.

The low-pressure ports shown in Figs. 2 and 3 can be modeled independently from the high-pressure ports because the reference state $V$ is specified as uniform and quiescent. It is interesting to note that the relative total pressure ratio vs relative total enthalpy ratio curves shown in Fig. 4 hold for all ideal wave cycles that employ the low-pressure-port gasdynamics shown in Fig. 3, and that establish the quiescent reference state $V$. It doesn't matter whether state $V$ is produced by a four-port wave rotor with either reverse-flow or through-flow wave cycles (discussed in the next section), or by a wave rotor with combustion internal to the rotor (cf., Ref. 3), or by other envisaged multiport cycles including wave engines with net shaft power output, the same relative total pressure ratio vs relative total enthalpy ratio relationship shown in Fig. 4 holds in the ideal limit. The next section describes the model for the high-pressure ports that establishes state $V$ in the present work.

### *High-Pressure Ports*

The gas in a rotor passage moving from state $Q$ to state $V$ experiences the gasdynamics shown at the high-pressure ports in Figs. 3a and 3b. Two different approaches are considered in the present work. In the through-flow wave cycle of Fig. 3a, the entire state $Q$ is discharged through the high-pressure exhaust port (that leads to the burner), located on the same end of the machine as the low-pressure exhaust port; in the reverse-flow cycle of Fig. 3b, state $C$ is discharged from the high-pressure exhaust port located on the same end of the machine as the low-pressure inlet port, and the state $D$ gas remains within the rotor.

*Through-flow wave cycle.* Consider a passage initially at the quiescent state $Q$. As the passage opens to the high-pressure inlet port (from the burner), the passage gas is compressed by the principal shock wave driven by the incoming port flow. In reality, while the passage gradually opens to the port flow (beginning at time $t_e$), an expansion wave moves into the port and reduces the total pressure of the incoming fluid. Simultaneously, compression waves, eventually steepening into a shock wave, enter the rotor passage. The principal shock wave compresses the passage (state $Q$) gas and allows the port flow to enter the passage. In the case of the through-flow wave cycle of Fig. 3a, the principal shock first compresses the state $C$ gas (fresh air) that entered the rotor in the low-pressure inlet port. In general, as a shock interacts with a contact, e.g., the interface between states $C$ and $D$ in the four-port wave cycle, a shock wave is transmitted and either a shock wave or an expansion wave is reflected. As the transmitted shock reaches the exhaust port end of the rotor, the passage opens to the high-pressure exhaust port $t_g$ while a reflected shock (in general of different strength than the transmitted shock) is reflected. The state $C$ and $D$ gases are recompressed by the reflected wave. The reflected shock wave also compresses the incoming flow from the burner. The passage closes off from the inlet port $t_f$, just as the reflected shock arrives at the inlet–port/rotor interface $x = 0$. This passage closing creates an expansion wave that brings the incoming flow to rest relative to the rotor. The outlet port is closed $t_h$ a time $t_V$ (i.e., the reference time) later. The twice-compressed states $C$ and $D$ gases now exit the rotor to the high-pressure exhaust port; the static pressure at the interface between the rotor and the high-pressure exhaust port is constant and uniform. This pressure is set by the expansion wave strength and the reference state $V$. The expansion wave effects a nonuniform velocity region at the exhaust port analogous to that in the low-pressure exhaust port and leads to a mixing loss in the high-pressure exhaust port.

*Reverse-flow wave cycle.* In the reverse-flow wave cycle shown in Fig. 3b, the principal shock first interacts with the undischarged state $D$ fluid, which entered through the high-pressure inlet port during the last passage charging sequence. Similar to the through-flow wave cycle discussed earlier, the principal shock interacts with the contact between state $C$ and $D$. The transmitted shock then reflects from the high-pressure exhaust port ($x = 0$), recompresses the state $C$ and $D$ gases, and compresses the gas from the burner that enters the rotor through the high-pressure inlet port. The passage closes off from the inlet port just as the reflected wave reaches the inlet–port/rotor interface. The expansion fan is generated that brings the incoming gas and the state $D$ gas to rest relative to the rotor. Note that because the state $D$ gas has already experienced a wave cycle, its entropy is greater than that of the new charge from the burner. The reference state $V$ internal energy (or $a_V^2$) is a mass-average of the internal energy of these two constituents. The expansion fan interacts with the contact between the state $C$ and $D$ gases, and creates a nonuniform velocity region as the state $C$ fluid is discharged to the exhaust port.

In both high-pressure port models, shock-wave speeds, compression ratios, and entropy production are calculated using the Rankine–Hugoniot relations. The strength of the expansion fan, which brings the high-pressure inlet port flow to rest in the uniform reference state $V$, sets the static pressure in the high-pressure exhaust port relative to $p_V$. This static pressure is that required to ensure that the principal shock wave, the reflected shock, and the expansion fan establish the prescribed wave diagrams (Fig. 3) with wave timing and flow properties that conserve mass and energy. The transmitted and reflected waves of shock/contact interactions are calculated to ensure continuous velocity and static pressure at the contact surfaces.

The overall solution involves an inner-loop search for the principal shock strength within an outer-loop search for the correct expansion fan strength. These searches set the high-pressure inlet port relative total pressure and enthalpy. The relative total enthalpy of the high-pressure exhaust port is then obtained from a relative energy balance for the entire machine. By knowing the timing, static pressure, relative total enthalpy, and mass discharged from the high-pressure exhaust port, the remaining properties can be obtained.

### Entropy Production Mechanisms

Important wave rotor entropy production mechanisms include viscous dissipation in 1) boundary layers and rotor wakes; 2) nonuniform outflow port flowfield mixing; and 3) separated flows caused by incidence, shock/boundary-layer interactions, and the gradual opening and closing of the rotor passages to the port flows.[15] Detailed descriptions of simple models for entropy production resulting from boundary layers, rotor wakes, nonuniform exhaust port flow mixing, incidence, and passage gradual opening and closing are provided in Ref. 19. The entropy produced in the shock waves is inherent to the shock relations discussed earlier. The relative motion between the rotor (and disks) and the stationary casing produces windage loss. Windage is expected to be negligible in pressure-exchangers given their relatively low rotative speeds; however, it can be significant in wave engines.[22] Passage-to-passage leakage and passage-to-casing-plenum leakage degrade machine performance by detrimentally redistributing mass and energy within the machine. In practice, leakage is mitigated by controlling the clearance gap between the rotor and the casing end walls. Conventional seals are used when necessary. The impact of leakage is neglected in the present work, but can significantly affect machine performance.[2] Machine performance is further degraded by heat transfer, which is also neglected in the results that follow. Finally, mixing and redistribution of hot and cold gases caused by multidimensional flow dynamics[15,16,23] adversely impact machine performance, but are not accounted for in the current model.

## Application to a Three-Port Wave Rotor

A three-port wave rotor is a pressure-exchanger that divides a medium total pressure $(p_t)_{in}$ inlet stream into two streams, one of higher total pressure $(p_t)_{hi}$ and one of lower total pressure $(p_t)_{lo}$. As shown in Fig. 2b, the wave diagram for the medium- and high-pressure ports of the three-port divider cycle is equivalent to the wave diagram for the high-pressure ports of the through-flow wave cycle (Fig. 3a); however, in the three-port, the mass discharged from the high-pressure exhaust port is equal to a fraction $\beta \equiv \dot{m}_{hi}/\dot{m}_{in}$ of the medium-pressure inlet flow, and may include part or all of the state $Q$ fluid, and part or none of the medium pressure inlet flow. The remaining mass, $(1 - \beta)\dot{m}_{in}$, is discharged to the low pressure port. Figure 5 shows a plot of the pressure ratios $(p_t)_{hi}/(p_t)_{in}$ and $(p_t)_{lo}/(p_t)_{in}$ as a function of $\beta$, for the Power Jets (R&D), Ltd. pressure-exchanger.[1] Figure 5 compares the predictions of the current model with experimental curves for the conditions shown: 6000 rpm, $T_{t,in} = 554°R$ (308 K), $(p_t)_{lo} \simeq 1$ atm (0.101 MPa). Figure 5 illustrates that the model predictions and the experimental data qualitatively agree. It is worth noting that each point along the curves of the present study represents an on-design wave rotor, i.e., one redesigned for that specific operating point, whereas the experimental curves are data from a single machine, running at constant rotor speed, with fixed port timing.[1] Further, the experiment used axially aligned porting that provided no preswirl, and the inlet flow was likely compressed by nonnegligible rotor work. Quantitative comparison suggests that the simple loss models do a fairly good job predicting appropriate entropy production levels. It was, however, expected that the on-design performance predicted by the present model would be greater than or equal to the actual (on- and off-design) machine performance. The lower predicted performance obtained at some operating points suggests that the predicted entropy production levels (e.g., boundary-layer loss) were too high. Although beyond the scope of the present work, this suggests modifying the loss models with empirical constants that are tuned through comparisons with experimental data.

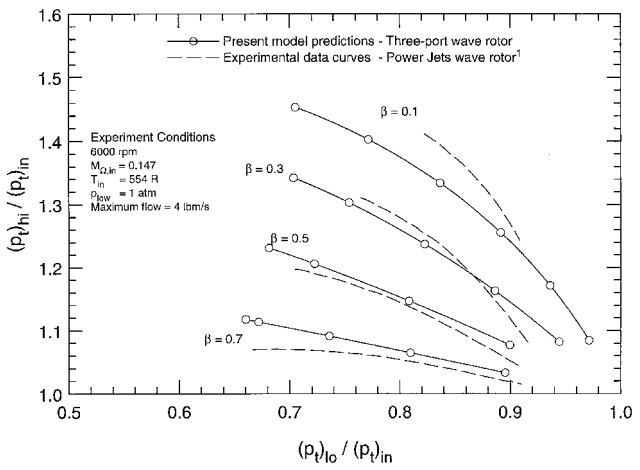


**Fig. 5 Comparison of three-port wave rotor performance curves computed by using the present model and from experimental data.[1]**

## Wave Rotor Design Application

The computational efficiency and accuracy of the described wave rotor model make it amenable to engine system design-point studies. Consider a small turboshaft engine with 2390°R (1330 K) turbine inlet temperature, and 5.0 lbm/s (2.27 kg/s) compressor discharge air at 7.77 atm (0.787 MPa) and 1080°R (600 K) (cf., Ref. 13). A pressure-exchanger topping unit for this engine is designed in this section. The maximum benefits of pressure-exchanger topping, in terms of engine net shaft power per mass flow rate and specific fuel consumption[13] are obtained when the wave rotor pressure ratio is maximized; therefore, the final design should provide the highest possible total pressure ratio $(p_t)_{out}/(p_t)_{in}$ at the total enthalpy ratio $HR$ = 2390°R/1080°R = 2.21 dictated by the engine.

Taussig[6] described a wave rotor design process and identified important nondimensional design parameters. Wilson and Paxson[24] used a similar analysis to obtain optimized wave rotor designs. In the present work, the expansion fan pressure ratio is first fixed at $\varepsilon = 0.4$ to ensure that $\alpha_m \geq 0.5$ (cf., Ref. 19). The design is carried out for a machine with two wave cycles (or duct sets) per revolution ($n = 2$) and an example coolant bleed fraction of $f_b = 6.9\%$. (In a more detailed analysis, the selection of the number of wave cycles per revolution might well be influenced by ducting weight, cooling, and aerodynamic issues that would impact a figure-of-merit for the overall engine system.) The rotor length $L_T$ and hub-to-tip ratio $R_H/R_T$ were varied parametrically. For each combination of rotor length and hub-to-tip ratio, the optimum rotor passage aspect ratio (chord length-to-tip-width) was determined by searching from some lower value (usually 10) incrementally upward. The pressure ratio, $(p_t)_{out}/(p_t)_{in}$, increases monotonically with passage aspect ratio up to a maximum. At each passage aspect ratio, an inner iteration determines the one rotor Mach number that satisfies the 5.0 lbm/s (2.27 kg/s) inlet mass flow rate requirement. Figures 6 and 7 present the results of this parametric analysis. (Note that the parametric analysis was carried out for zero coolant bleed fraction.) Figure 6 compares the pressure ratio vs rotor length for wave rotors of various hub-to-tip ratios. Performance is highest near the 10 in. (25.4 cm) rotor length on the 0.8 hub-to-tip ratio curve; however, nearly comparable performance levels are found between the 8 in.

**Table 2 Wave rotor design-point values[a]**

| Parameter | Value | Parameter | Value |
|---|---|---|---|
| Absolute total enthalpy ratio | 2.212 | $t_{vt}$ ms | 0.234 |
| Absolute total pressure ratio | 1.204 | Nondimensional opening time | 0.409 |
| Expansion fan pressure ratio | 0.4 | Nondimensional wave cycle time | 9.72 |
| Ratio of specific heats | 1.315 | Total rotor passages | 44 |
| Wave cycles per revolution | 2 | Rotor tip radius, in. (cm) | 3.35 (8.51) |
| Rotor length | 7.0 | Passage width at tip, in. (cm) | 0.443 (1.13) |
| Hub-to-tip ratio | 0.667 | Rotor passage height, in. (cm) | 1.12 (2.84) |
| Passage aspect ratio | 15.8 | Rotor angular speed, rpm | 13,167 |
| Rotor tip Mach number | 0.247 | Rotor tip speed, ft/s (m/s) | 385 (117) |
| Blade thickness/passage width at tip | 0.08 | Rotor equivalent tip speed, ft/s (m/s) | 267 (81.4) |

*Wave rotor design for 5.0 lbm/s (2.27 kg/s) turboshaft engine topping cycle with 2390°R (1330 K) turbine inlet temperature, 1080°R (600 K) and 7.77 atm (0.787 MPa) compressor discharge, and 6.9% coolant bleed extraction from wave rotor.

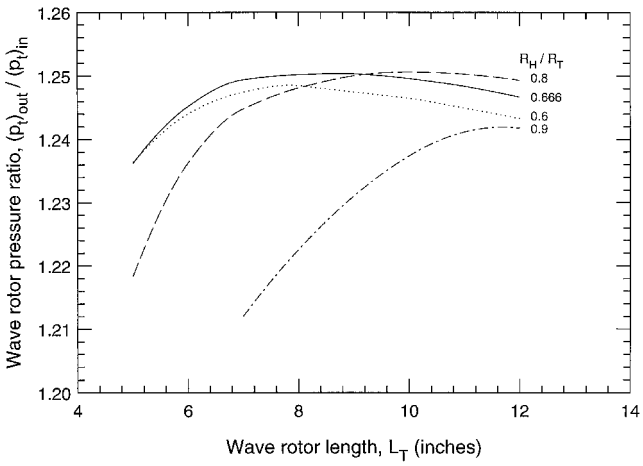


**Fig. 6 Wave rotor pressure ratio $(p_t)_{out}/(p_t)_{in}$ as a function of rotor length $L_T$ and hub-to-tip ratio $R_H/R_T$ for a 5 lbm/s (2.27 kg/s) machine.**

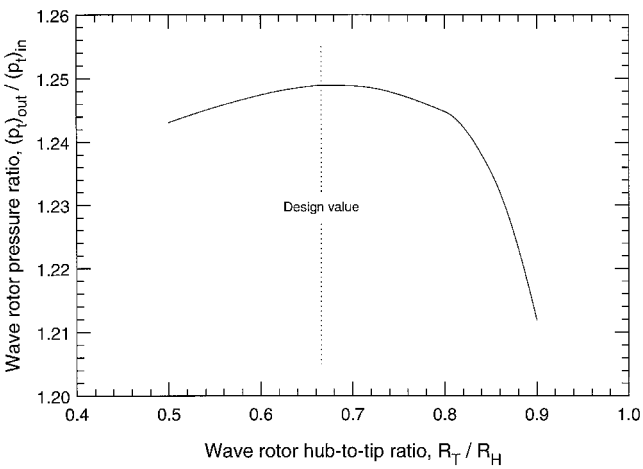


**Fig. 7 Wave rotor pressure ratio $(p_t)_{out}/(p_t)_{in}$ as a function of hub-to-tip ratio $R_H/R_T$ at a 7 in. (17.8 cm) rotor length $L_T$.**

(20.3 cm) and 9 in. (22.9 cm) rotor lengths on the 0.667 curve. The rotor tip radius increases nearly quadradically with increasing hub-to-tip ratio, and the optimum rotor length increases as the hub-to-tip ratio increases; therefore, the 0.667 rotor curve was selected to minimize the rotor size and weight while attaining nearly maximum performance. Further, although the optimum pressure ratio on the 0.667 hub-to-tip ratio curve occurs near the 9 in. (22.9 cm) rotor length, comparable performance is realized at 7 in. (17.8 cm); again, for weight considerations, the 7 in. (17.8 cm) length is selected for the design point. In Fig. 7 the rotor length is fixed at 7 in. (17.8 cm), and the hub-to-tip ratio is varied to narrow in on the optimum. The maximum pressure ratio of nearly 1.25 occurs at an optimum hub-to-tip ratio of 0.667. The impact of 6.9% coolant bleed extraction (see discussions in Refs. 13 and 19) on wave rotor performance was to reduce the pressure ratio to 1.204. Other design-point values are provided in Table 2.

## Summary

A wave rotor model based on macroscopic mass, momentum, and energy balances, one-dimensional gasdynamic wave processes, and loss models for wave rotor entropy production mechanisms was described. A comparison of model predictions with three-port divider cycle experimental data indicated that entropy production was slightly overpredicted by the simple loss models. Comparisons with one-dimensional CFD calculations showed that the model accurately predicts the ideal performance (i.e., that which accounts for entropy production only in shock waves and in mixing nonuniform exhaust port flowfields) of wave rotors for gas turbine engine topping applications. A pressure-exchanger design example illustrated the applicability of the model to wave rotor design and optimization. The wave rotor model requires minimal computational investment, making it well suited for the rapid assessment of topping cycle benefits and other tradeoffs associated with integrating wave rotors into gas turbine engines.

## Acknowledgments

The author is grateful for the valuable suggestions offered by Louis M. Larosiliere, of the U.S. Army Research Laboratory, with regards to this paper. The author also thanks Jack Wilson, of NYMA, Inc., and Daniel E. Paxson, of NASA Lewis Research Center, for interesting discussions on wave rotor and for assistance with model validation.

## References

[1]Kentfield, J. A. C., "The Performance of Pressure-Exchanger Dividers and Equalizers," *Journal of Basic Engineering*, Vol. 91, Sept. 1969, pp. 361–370.

[2]Wilson, J., and Fronek, D., "Initial Results from the NASA Lewis Wave Rotor Experiment," AIAA-93-2521, June 1993; also NASA TM-106148, May 1993.

[3]Goldstein, A. W., Klapproth, J. F., and Hartmann, M. J., "Ideal Performance of Valved-Combustors and Applicability to Several Engine Types," *Transactions of the American Society of Mechanical Engineers*, Vol. 80, July 1958, pp. 1027–1036.

[4]Meyer, A., "Recent Developments in Gas Turbines," *Mechanical Engineering*, Vol. 69, No. 4, 1947, pp. 273–277.

[5]Zauner, E., Chyou, Y.-P., Walraven, F., and Althaus, R., "Gas Turbine Topping Stage Based on Energy Exchangers: Process and Performance," American Society of Mechanical Engineers, 93-GT-58, May 1993.

[6]Taussig, R. T., "Wave Rotor Turbofan Engines for Aircraft," edited by J. F. Sladky Jr., *Machinery for Direct Fluid-Fluid Energy Exchange*, AD-07, American Society of Mechanical Engineers, New York, Dec. 1984, pp. 9–45.

[7]Rose, P. H., "Potential Applications of Wave Machinery to Energy and Chemical Processes," edited by A. Lifshitz and J. Rom, *Shock Tubes and Wave, Proceedings of the 12th International Symposium on Shock Tubes and Waves*, The Magnes Press, Jerusalem, Israel, July

1979, pp. 3–30.
[8]Sladky, J. F., Jr. (ed.), *Machinery for Direct Fluid-Fluid Energy Exchange*, AD-07, The American Society of Mechanical Engineers, New York, Dec., 1984.
[9]Shreeve, R. P., and Mathur, A. (eds.), *Proceedings of the 1985 ONR/NAVAIR Wave Rotor Research and Technology Workshop*, Naval Postgraduate School, 67-85-008, Monterey, CA, May 1985.
[10]Azoury, P. H., *Engineering Applications of Unsteady Fluid Flow*, Wiley, New York, 1992.
[11]Kentfield, J. A. C., *Nonsteady, One-Dimensional, Internal, Compressible Flows*, Oxford Univ. Press, Inc., Oxford, England, UK, 1993.
[12]Weber, H. E., *Shock Wave Engine Design*, Wiley, New York, 1995.
[13]Welch, G. E., Jones, S. M., and Paxson, D. E., "Wave-Rotor-Enhanced Gas Turbine Engines," *Journal of Engineering for Gas Turbines and Power*, Vol. 119, No. 2, 1997, pp. 469–477.
[14]Paxson, D. E., "Comparison Between Numerically Modeled and Experimentally Measured Wave-Rotor Loss Mechanisms," *Journal of Propulsion and Power*, Vol. 11, No. 5, 1995, pp. 908–914.
[15]Welch, G. E., and Chima, R. V., "Two-Dimensional CFD Modeling of Wave Rotor Flow Dynamics," *Proceedings of the 11th Computational Fluid Dynamics Conference*, Part 1, 1993, pp. 234–247; also NASA TM-106261, Feb. 1994.
[16]Larosiliere, L. M., "Wave Rotor Charging Process: Effects of Gradual Opening and Rotation," *Journal of Propulsion and Power*, Vol. 11, No. 1, 1995, pp. 178–184.
[17]Rudinger, G., *Wave Diagrams for Nonsteady Flow in Ducts*, D. Van Nostrand Co., New York, 1955, pp. 186–193.
[18]Foa, J. V., *Elements of Flight Propulsion*, Wiley, New York, 1960, pp. 161–166.
[19]Welch, G. E., "Macroscopic Balance Model for Wave Rotors," AIAA Paper 96-0243, Jan. 1996; also NASA TM-107114 and Army Research Lab., TR-925, Jan. 1996.
[20]Mathur, A., "A Brief Review of the G. E. Wave Engine Program (1958–1963)," edited by R. P. Shreeve, and A. Mathur, *Proceedings of the 1985 ONR/NAVAIR Wave Rotor Research and Technology Workshop*, Naval Postgraduate School, 67-85-008, Monterey, CA, May 1985, pp. 171–193.
[21]Berchtold, M., "The Comprex as a Topping Spool in a Gas Turbine Engine for Cruise Missile Propulsion," edited by R. P. Shreeve and A. Mathur, *Proceedings of the 1985 ONR/NAVAIR Wave Rotor Research and Technology Workshop*, Naval Postgraduate School, 67-85-008, Monterey, CA, May 1985, pp. 284–290.
[22]Pearson, R. D., "A Gas Wave-Turbine Engine Which Developed 35 HP and Performed over a 6:1 Speed Range," edited by R. P. Shreeve and A. Mathur, *Proceedings of the 1985 ONR/NAVAIR Wave Rotor Research and Technology Workshop*, Naval Postgraduate School, 67-85-008, Monterey, CA, May 1985, pp. 125–170.
[23]Keller, J. J., "Some Fundamentals of the Supercharger Comprex®," edited by J. F. Sladky Jr., *Machinery for Direct Fluid-Fluid Energy Exchange*, AD-07, American Society of Mechanical Engineers, New York, Dec. 1984, pp. 47–54.
[24]Wilson, J., and Paxson, D. E., "Wave Rotor Optimization of Gas Turbine Engine Topping Cycles," *Journal of Propulsion and Power*, Vol. 12, No. 4, 1996, pp. 778–785.